


ARTICLE



Integrative multi-omics reveal NSUN2 facilitates glycolysis and histone lactylation-driven immune evasion in renal carcinoma

Kunpeng Wang¹, Fanyi Kong¹, Xue Han², Yunlai Zhi¹, Hai Wang¹ ²✉, Chuanli Ren³✉ and Hui Wang¹✉

© The Author(s), under exclusive licence to Springer Nature Limited 2025

Clear cell renal carcinoma (ccRCC) is the most prevalent and aggressive subtype of kidney cancer. Targeting ccRCC metabolism is a promising therapeutic strategy, and some metabolic targets are currently undergoing clinical trials. Here, we collected multiple ccRCC clinical cohorts, including bulk RNA sequencing and single-cell sequencing datasets, to investigate mitochondrial metabolic genes' prognostic and therapeutic potential. Integrating 10 machine learning algorithms, we constructed 117 predictive models, with the optimal model selected and defined as Mitoscore for patient stratification and treatment. Furthermore, NSUN2, an RNA 5-methylcytosine (m5C) methyltransferase, was identified as the most important gene in the model and selected for further gene function experiments in vitro and in vivo. NSUN2 promoted cell proliferation, migration, and invasion; reprogrammed glycolysis metabolism and histone lactylation levels via maintaining NEO1 mRNA stability. In addition, NSUN2 increased PD-L1 expression in tumor cells via the MYC/POM121/CD274 axis in a lactylation-dependent manner. Knockdown of NSUN2 enhanced CD8 T cell killing effects in vitro, along with TNF- α + T cell infiltration in vivo. These results highlight that mitochondrial genes are optional therapeutic targets and prognostic markers; NSUN2 promotes mitochondrial glycolysis and histone lactylation in an m5C-dependent manner, thereby resulting in PD-L1-mediated immune escape, which elucidates novel NSUN2-mediated crosstalk between glycolysis and immune evasion.

Genes & Immunity; <https://doi.org/10.1038/s41435-025-00336-4>

INTRODUCTION

Renal cell carcinoma (RCC) primarily consists of two histological subtypes: ccRCC (originating from the epithelial cells of the proximal renal tubule) and non-clear cell RCC, with ccRCC being the most prevalent and aggressive, accounting for roughly 75% of RCC cases [1]. Non-clear cell RCC comprises papillary RCC (10–15%), chromophobe RCC (about 5%), and other rare subtypes (less than 1%) [2]. Moreover, another categorical-histological classification divides them into five subtypes, including clear cell, papillary type I, papillary type II, chromophobe, and oncocytoma renal cell carcinoma [3], while RCC can be classified into 10 subtypes according to its histology and genetics [4]. Although renal cancer comprises just 2% of all malignancies worldwide, its incidence has been rising at an annual rate of around 1% [5]. Patients with metastatic renal cancer suffer a worse prognosis, with a 5-year survival rate below 10% [4]. Therapeutic approaches for RCC consist mainly of adjuvant and neoadjuvant (surgery, chemotherapy, radiotherapy), immunotherapy, and combination therapy [6]. The first-line treatment options include tyrosine kinase inhibitors (TKIs), VEGFR (vascular endothelial growth factor receptor)-targeted therapy, and immune checkpoint inhibitors (ICIs) [7, 8]. The current well-known combination therapy for RCC treatment mainly involves the combination of ICI with TKI or VEGF inhibitors [9, 10]. Although popular anti-angiogenic therapies and emerging immunotherapies have improved survival time for

patients with kidney cancer [11, 12], significant challenges persist, including acquired resistance and poor responses to immunotherapy [13]. Therefore, the development of novel therapeutic strategies is essential to expand treatment substitutability for RCC treatment.

Metabolic reprogramming is widely regarded as a critical hallmark of cancer, with significant implications for diagnosis, prognosis, and the response of targeted therapies [14]. The RCC has been described as a disease of metabolic disorder [3, 15]. Genomic and proteomic analyses of 232 Chinese ccRCC patients revealed significant metabolic and immune dysregulation [1]. The ccRCC tumors demonstrated an increased reliance on glycolysis for energy supply, instead of oxidative phosphorylation (OXPHOS) [15]. OXPHOS inhibition enhanced the efficiency of immune checkpoint blockade in preclinical [16]. Metabolomic studies have shown that ccRCC exhibited higher glycolytic levels in comparison to corresponding normal tissues [15]. Recent research has inspired us to explore the therapeutic vulnerabilities of mitochondria by modulating mitochondrial metabolism [17]. Targeting ccRCC metabolic reprogramming, some targets have been proven effective and are currently undergoing clinical trials, including but not limited to hypoxia-inducible factor 1- α (HIF-2 α) [18], glutaminase [19], indoleamine-2,3-dioxygenase-1 (IDO1) [20]. Moreover, ferroptosis, as a lipid metabolism-dependent cell death, exhibited significant and promising therapeutic potential in

¹Department of Urology, The Affiliated Lianyungang Hospital of Xuzhou Medical University, The first People's Hospital of Lianyungang, Jiangsu, China. ²Department of Image, The Affiliated Huai'an Hospital of Xuzhou Medical University and The Second People's Hospital of Huai'an, Huai'an, China. ³Department of Laboratory Medicine, Northern Jiangsu People's Hospital Affiliated to Yangzhou University, Yangzhou, China. ✉email: HW1986_edu@163.com; renchl@163.com; wh2796329@sina.com

Received: 21 December 2024 Revised: 30 April 2025 Accepted: 12 May 2025

Published online: 24 May 2025

ccRCC, even in RCC [21, 22]. Despite encouraging advancements in elucidating metabolic dysfunction in RCC and its molecular contributions to cancer initialization, the therapeutic vulnerabilities of mitochondrial genes have not been thoroughly investigated.

To exploit the potential role of mitochondrial genes in the prognosis and treatment of clear cell renal cell carcinoma, we collected clinical cohorts for data mining and integrated ten machine learning algorithms to build prognostic models. The best model, named Mitoscore, demonstrated excellent predictive performance in assessing patient survival outcomes. Mechanistically, heterogeneity in immune infiltration and metabolic profiles significantly affected the prognosis between different mitochondrial signature subgroups. Further, we screened a key gene, NSUN2 (NOP2/Sun-domain family member 2), an RNA 5-methylcytosine (m5C) methyltransferase, which served as an independent prognostic factor and the most important variable in the model. We examined its molecular functions both in vitro and in vivo (Fig. 1A). In this study, NSUN2 driven ccRCC progression by enhancing glycolysis and promoting PD-L1 (programmed cell death ligand 1)-mediated immune evasion through upregulation of histone H3 lysine-18 lactylation (H3K18la). NSUN2 bridges glycolysis and immune evasion, suggesting that co-targeting glycolytic metabolism and the tumor immune microenvironment in cancer is a promising alternative therapeutic strategy.

MATERIALS AND METHODS

Bulk RNA-sequencing analysis

Data collection and processing. The 1136 annotated mitochondrial genes were released by the MitoCarta3.0 [23]. RNA sequencing data from The Cancer Genome Atlas-Kidney Renal Clear Cell Carcinoma (TCGA-KIRC) cohort (501 tumor tissues and 101 adjacent normal tissues) and paired clinical data were retrieved from the Genomic Data Commons Data Portal (<https://portal.gdc.cancer.gov/>). In addition, 101 clear cell renal cell carcinoma samples (E-MTAB cohort) were deposited in BioStudies (<https://www.ebi.ac.uk/biostudies/arrayexpress/studies/E-MTAB-1980>) [24]. The International Cancer Genome Consortium data portal (ICGC, <https://dcc.icgc.org/>) provided expression profiles and clinical data for the KIRC cohort (ICGC-KIRC, 91 cases) [25]. Data from the RNA expression matrix and clinical follow-up information of the GSE29609 dataset were retrieved from the NCBI-GEO database (<https://www.ncbi.nlm.nih.gov/geo/>). The TCGA pan-cancer cohort (33 types of cancer) was downloaded from the UCSC Xena web server (<https://xena.ucsc.edu/>).

Duplicate samples were removed, and expression matrices were normalized using log2 transformation. Survival times were scaled in years, and Kaplan-Meier analysis was used to evaluate the correlation between expression levels and survival outcomes. The Receiver Operating Characteristic (ROC) curve was introduced to assess the predictive accuracy for patient survival status, with the Area Under Curve (AUC) ranging from 0 to 1, with a value of 1 indicating perfect accuracy. Cox univariate analysis was performed to evaluate the association between gene expression and prognostic survival. Patients in each cohort were classified into high-risk and low-risk groups based on the median Mitoscore.

Building and visualizing predictive models. The above three bulk RNA-sequencing cohorts were utilized to construct prognostic models for survival prediction, employing ten machine learning algorithms: Least Absolute Shrinkage and Selection Operator (LASSO), Random forests (RSF), Elastic network (Enet), Stepwise Cox (StepCox), CoxBoost, Partial Least Squares Regression for Cox (plsRcox), Supervised Principal Components (superc), Generalized Boosted Regression Models (GBM), survival support vector machine (survivalsvm), and Ridge regression (Ridge). These methods were implemented using the R package Mime [26]. 1038 mitochondrial genes were retrieved from the TCGA cohort, and further univariate COX analysis screened 249 candidate genes that were significantly associated with patient prognosis, and 117 combination models were constructed based on the expression matrix of prognosis-related genes.

Tumor microenvironment analysis. The immune infiltration in the tumor microenvironment of the TCGA cohort was analyzed using the R package

CIBERSORT to investigate differences in immune cell fractions [27]. This method deconvoluted the proportions of 22 immune cell types based on RNA expression profiles, including several key cell types involved in tumor immunity (B cells, CD8+ T cells, CD4+ T cells, etc.).

Single-cell transcriptomics analysis

Data collection and handling. The annotated single-cell transcriptome data set for TJ-RCC was obtained from a previous study [28]. The “Seurat” package was employed to process and visualize the above single-cell RNA sequencing (scRNA-seq) dataset [29]. In addition, the Mitoscore for each single cell was calculated using the “AddModuleScore” function loaded in the “Seurat” package, with key genes from the Mitoscore model as input, according to the previous study [30, 31]. The gene expression profiles across various cell types were depicted using the “DotPlot” function. Tumor cells were categorized into NSUN2+ (positive) and NSUN2- (negative) clusters, determined by whether the NSUN2 expression in tumor cells surpassed a threshold of 0.

Metabolism analysis for scRNA-seq. The scMetabolism package was introduced to assess metabolic pathway activity within scRNA-seq datasets through a scoring approach [32]. Furthermore, the Python-based algorithm scFEA, which utilized a graph neural network, was implemented to estimate metabolic flux at the single-cell level [33].

Cellular and animal experiments

Cell culture. The human renal cell line 786-O and murine renal carcinoma cell line Renca were acquired from Procell (CL-0568, Wuhan Pricella Biotechnology Co., Ltd., China) and cultured in RPMI-1640 medium containing 10% fetal bovine serum and 1% penicillin-streptomycin, and were kept in a humidified incubator at 37 °C with 5% CO₂ atmosphere. To generate stable knockdown cell lines, a customized lentivirus (HanBio Technology, Shanghai, China) was used to infect the Renca cells for 48 hours, followed by a two-week selection process using 1 µg/mL puromycin.

Cell proliferation assay. Cell viability was evaluated by seeding 2000 cells into each well of a 96-well culture plate. Following cell adhesion, the cell viability test was conducted at specified time points using a 10% CCK-8 reagent, with absorbance measured at 450 nm through the plate reader (Varioskan LUX, Thermo Fisher Scientific, USA). For colony formation assays, 500 cells were seeded in 24-well plates and incubated for one week. Afterward, the cells were fixed with 4% paraformaldehyde and stained using 0.1% crystal violet (V5265, Merck KGaA, Darmstadt, Germany). Colony images were captured, and the clonal area was quantified with ImageJ software.

Migration and invasion assay. Cells were cultured in chambers with an 8 µm diameter (723301, NEST Biotechnology Co., Ltd, China) for 3 days to conduct the cell migration assay. Following this, fixation of the cells was performed using 4% paraformaldehyde, then stained with 0.1% crystal violet. The upper layer of cells was gently removed with a cotton swab, allowing for visualization of the submembrane layer, which was then photographed using the Axio Observer 7 microscope (ZEISS, Germany). For the invasion assay, cells were seeded into chambers coated with matrix gel (211212, NEST Biotechnology Co., Ltd) and treated like that of the migration assay.

Western Blotting. Total proteins were extracted using the RIPA lysis buffer kit (AR0102, Boster Biological Technology, Wuhan, China) and quantified with a bicinchoninic acid kit (AR1189, Boster). Denatured proteins were separated by sodium dodecyl sulfate-polyacrylamide gel electrophoresis (SDS-PAGE). Following separation, the proteins were transferred to polyvinylidene difluoride (PVDF) membranes, which were then blocked in a 5% bovine serum albumin (BSA) for 1 hour at room temperature. The membranes were covered by primary antibodies overnight at 4 °C (Supplementary Table 1). Afterward, a secondary antibody (#BA1039, Boster) was applied to amplify the signal of the primary antibodies, and then these blots were visualized using a chemiluminescent substrate kit (32106, Thermo Scientific, USA).

T-cell killing assay. Primary CD8+ T cells were isolated using a mouse CD8 T cell selection kit (480136, BioLegend, Inc., USA) and subsequently activated with anti-CD3 (300301, BioLegend) and anti-CD28 (302901,

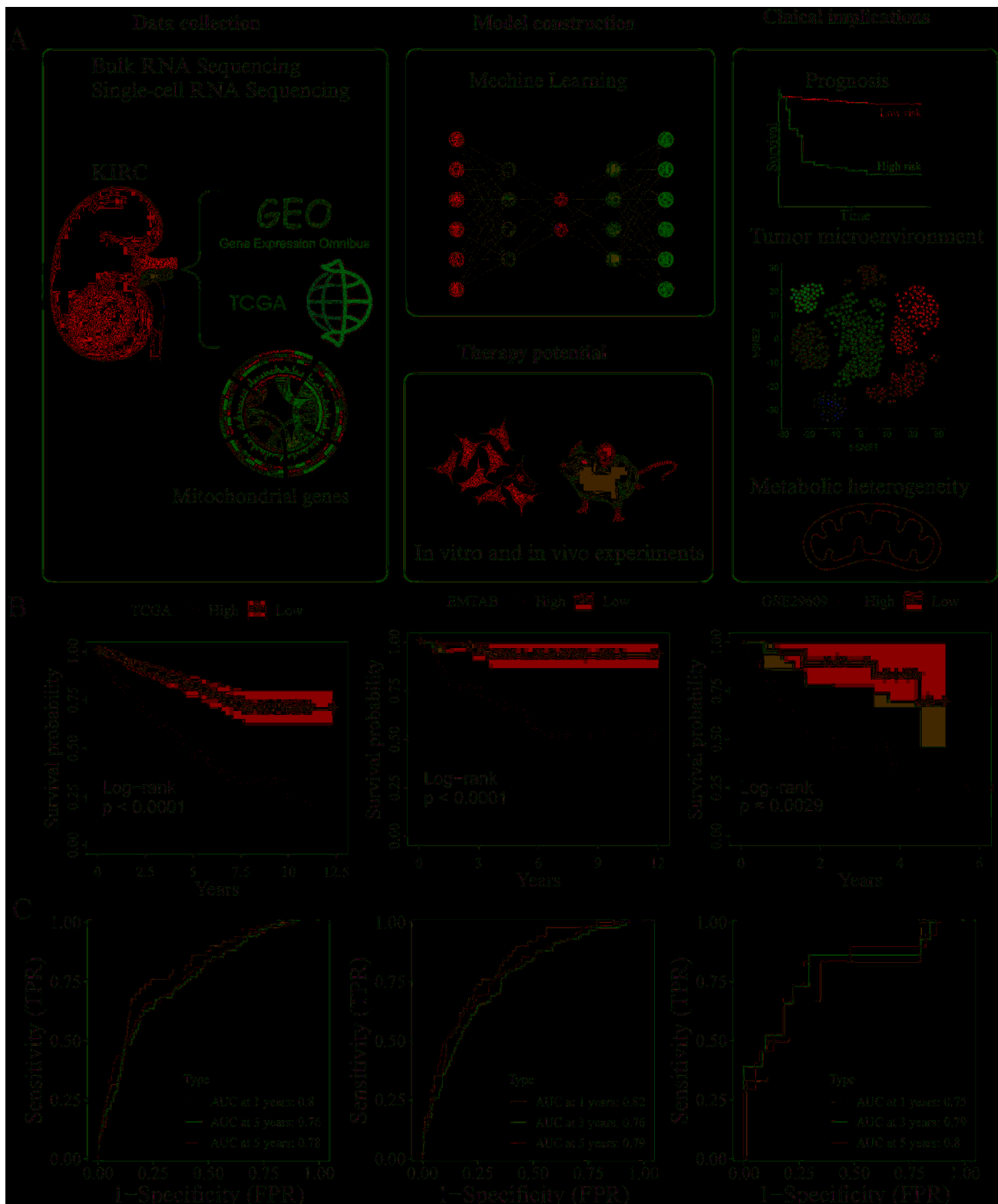


Fig. 1 Research overview and the predictive performance of the Mitoscore model. **A** Workflow of this study. The survival curve (**B**), the Receiver Operating Characteristics (ROC) curve (**C**) in TCGA, EMTAB, and GSE29609 datasets.

BioLegend) for 2 weeks. After activation, these T cells were added to 96-well plates that had been pre-seeded with 2,000 tumor cells at a ratio of 20:1 (T cells: tumor cells) and co-cultured for 48 hours. After this incubation, floating cells were removed by changing the medium, and then adherent live cells were stained with Hoechst 33342 (C1027, Beyotime Biotech,

China). The Celigo® Image Cytometer (Nexcelom Bioscience, USA) was then used to count the cell number in each well in fluorescent mode.

ATP, lactate, and ECAR assay. Cellular ATP and lactate concentrations were quantified using the ATP chemiluminescence assay kit (E-E-BC-F002,

Elabscience, Wuhan, China) and the L-lactic acid colorimetric assay kit (E-BC-K044-M, Elabscience), adhering to the manufacturer's protocols. The extracellular acidification rate (ECAR) was measured with the Agilent Seahorse XFe24 analyzer, utilizing the Seahorse XF Glycolytic Rate Assay Kit (103344-100, Agilent, USA) to assess mitochondrial glycolysis, following the manufacturer's guidelines (glucose:10 mM, oligomycin:0.5 μ M, and 2-DG:100 mM) [34].

RT-qPCR (quantitative reverse transcriptional PCR). The total RNA was extracted using the MolPure Cell/Tissue Total RNA Kit (19221ES50, YEASEN, Shanghai, China). The Hifair AdvanceFast 1st Strand cDNA Synthesis SuperMix for qPCR kit (11156ES10, YEASEN) was used for performing reverse transcription reaction to synthesize cDNA, and its concentration was measured by the NanoDrop microvolume spectrophotometers (Thermo Fisher Scientific, USA). RT-qPCR analysis was performed with the LightCycler 480 (Roche Applied Science, USA) using the indicated primers (Supplementary Table 2) and Hieff qPCR SYBR Green Master Mix (11201ES08, YEASEN). For RNA stability analysis, human kidney cancer cells were seeded into a six-well plate and allowed to adhere. After treatment with actin D (1 μ g/mL, S8964, Selleck) for a specified period of time, total RNA was collected and NEO1 mRNA expression was quantified using the rt qPCR method described above.

Animal experiment. The animal experiments were approved and supervised by the Animal Ethics Committee of the Affiliated Lianyungang Hospital of Xuzhou Medical University. The female BALB/c mice, aged 6 to 8 weeks, were acquired by GemPharmatech (Nanjing, China) and housed in accordance with the guidelines set by the Animal Ethics Committee. The mice were maintained in a specific pathogen-free laboratory animal house, with unrestricted access to food and water. After being randomly grouped, each mouse received an injection of 1×10^5 Renca cells to establish xenograft tumors. Tumor volumes were measured through the formula: $0.5 \times \text{length} \times \text{width}^2$.

Flow cytometry. Fresh tumor tissues were separated into two fractions for pathological analysis and flow cytometry, respectively. The tumor tissues were mechanically dissociated and digested to obtain single-cell suspensions, which were then filtered through a 70-micron cell strainer. To activate tumor T cells for the release of intracellular factors, the Cell Activation Cocktail (423303, BioLegend, USA) was applied for a 6-hour treatment. Following this, cells were blocked with Anti-Mouse CD16/CD32 (553141, BD Pharmingen, USA) and subsequently stained with the Zombie NIR Fixable Viability Kit (423105, BioLegend), Brilliant Violet 711 anti-mouse CD45 (103147, BioLegend), Brilliant Violet 510 anti-mouse CD3 (100233, BioLegend), Alexa Fluor 700 anti-mouse CD4 (100429, BioLegend), FITC anti-mouse CD8a (100705, BioLegend), and PE anti-mouse TNF- α (506305, BioLegend). Fluorescence signals were acquired using the NovoCyte Flow Cytometer (3005, Agilent Technologies, Inc., USA), and the data of fluorescence signals were analyzed and visualized with FlowJo software (version 10.8.1).

Histopathology. According to previous literature [35], tumor tissues were prepared as paraffin blocks, and an automated hematoxylin-eosin (HE) stainer (VENTANA HE 600, Roche Diagnostics, USA) was employed for the visualization of nuclear and cytoplasmic distribution in the mice tumor tissues. Before dewaxing and hydration, the paraffin-embedded tissues were sliced into 5 μ m sections. Antigen retrieval was performed using citrate solution (AR0024, Boster Biological Technology, Wuhan, China), followed by a blocking step with 5% bovine serum albumin (AR0004, Boster). The samples were incubated overnight with primary antibodies at 4°C, then followed by the incubation of secondary antibodies at room temperature for 1 hour. Staining with diaminobenzidine (DAB) was executed using a DAB kit (AR1027, Boster), followed by staining of the nuclei with hematoxylin.

Statistical analysis

The software GraphPad Prism 9.0 was used for statistical analysis of experimental data. Data with a normal distribution are shown as mean \pm standard deviation, and the T-test was used to compare two groups. All cellular experiments were repeated at least three times biologically, unless otherwise labeled. One-way ANOVA assessed differences in means across multiple groups. For data that did not follow a normal distribution, the Wilcoxon test was applied for comparisons between two groups, while the Kruskal-Wallis test was utilized for the

comparison among multiple subgroups. The *p*-value of less than 0.05 was considered significant in statistics.

RESULTS

Integrating machine learning algorithms to develop prognostic models

Initially, to identify the optimal models for maximizing the prognostic potential of mitochondrial genes, we integrated 10 machine learning algorithms to construct 117 models. Among these, StepCox[forward]+Ridge demonstrated the best predictive performance, both in the TCGA training set and other additional independent validation datasets, and was designated the Mitoscore model (Fig. S1). Based on this signature, patients were classified into high-risk (Mitoscore-high) and low-risk (Mitoscore-low) subgroups. The Mitoscore-high subgroup exhibited worse prognostic survival compared to the Mitoscore-low subgroup (Fig. 1B). ROC curve analysis confirmed that Mitoscore exhibited excellent predictive accuracy for patient survival outcomes (Fig. 1C).

The characteristics of metabolic and immune microenvironment in Mitoscore subtypes

To investigate the molecular mechanisms underlying survival differences between the Mitoscore subgroups, we performed gene enrichment analysis and metabolic pathway analysis between the high- and low-risk groups (Figs. 2, S2). Gene ontology (GO) analysis indicated that immune-related pathways were enriched in the different risk subgroups, including the humoral immune response (Fig. 2A). We further examined immune cell infiltration and found that Mitoscore-high patients had poorer immune infiltration, as evidenced by lower CD4+ and CD8+ T cell ratios compared to Mitoscore-high patients (Fig. 2B, C). To explore the causes of these immune cell infiltrates, we analyzed the expression of immune-related molecules in the two groups (Fig. S2). High expression of multiple immunosuppressive molecules was observed in the Mitoscore-high subgroup, with notable upregulation of the classical immune checkpoint CD274 (encoding PD-L1) (Fig. 2D). Additionally, single-cell metabolic pathway analysis confirmed that Mitoscore-high tumor cells exhibited enhanced oxidative phosphorylation and glycolysis levels (Fig. S3A). Further single-cell metabolic flow analysis showed that Mitoscore-high tumor cells had elevated lactate and glucose levels (Fig. S3B, C). These findings suggest that elevated immune checkpoint expression and glycolysis contribute to the poor prognosis observed in Mitoscore-high patients.

Screening and identification of a key gene: NSUN2

To screen for the most important candidate gene in the Mitoscore model, the top 50 most important genes and their relationship with clinical features were shown (Fig. 3A). NSUN2 had the highest significance and a univariate Cox analysis implied that NSUN2 was significantly relevant with unfavorable prognosis among all model genes (Fig. 3B). Next, single-cell pathway activity analysis showed that NSUN2 high-expressing cells had higher levels of metabolism, including oxidative phosphorylation and glycolysis, and the same trend was also observed in tumor cells relative to epithelial cells (Fig. S4). NSUN2+ cells also had higher levels of lactate and glucose metabolism streams, compared to NSUN2- tumor cells (Fig. S5).

Subsequently, we assessed the expression pattern and clinical correlation of NSUN2. NSUN2 was significantly and highly expressed in tumor tissues, compared to normal tissues in TCGA-KIRC (Fig. 4A). Single-cell dataset analysis indicated that NSUN2 was predominantly located in malignant tumor cells (Fig. 4B, C). Survival analysis showed that higher NSUN2 levels were associated with poorer prognostic outcomes (Fig. 4D). Its expression was also associated with tumor pathologic stage and

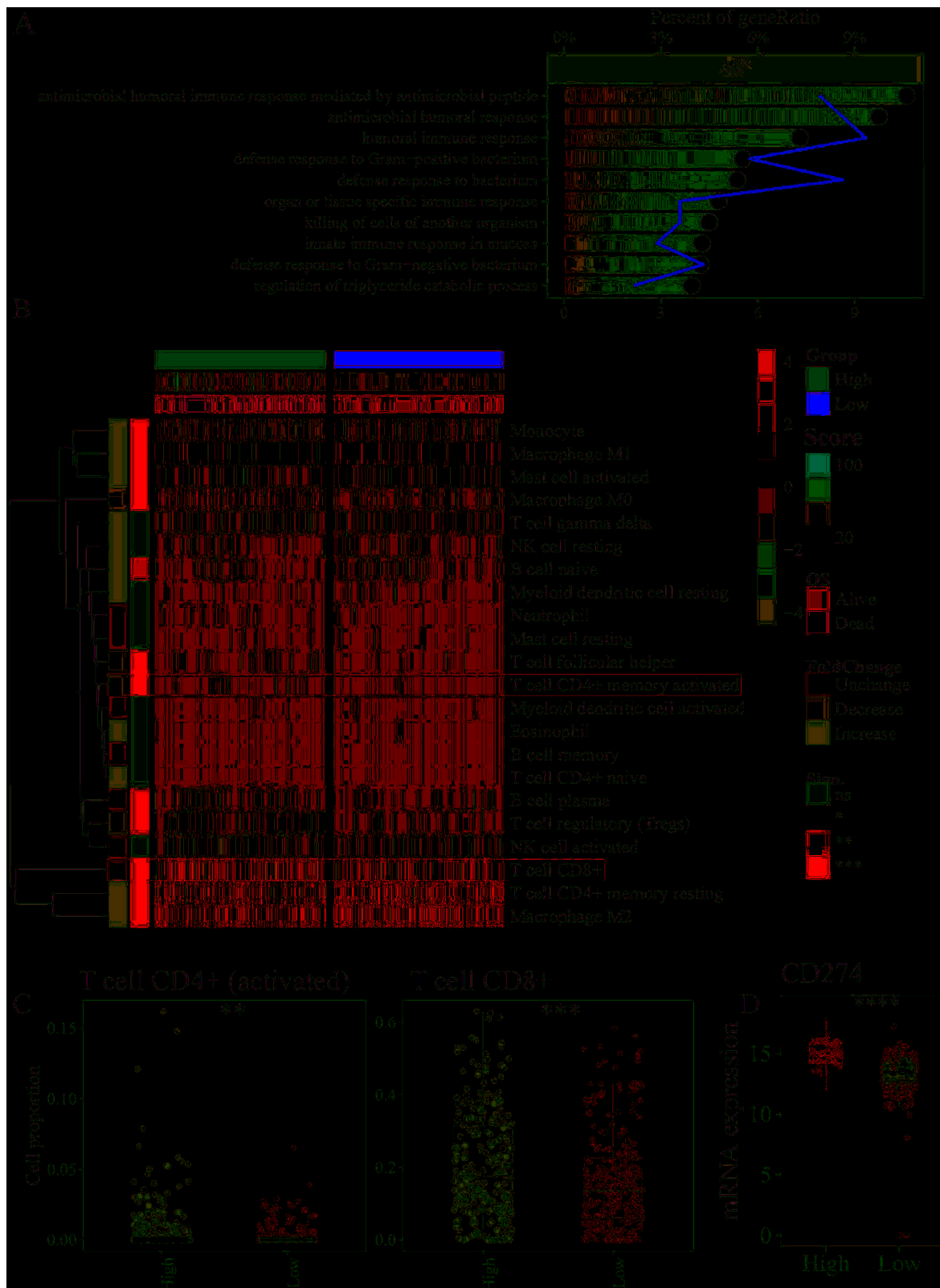


Fig. 2 The expression heterogeneity of Mitoscore determinates patient's tumor immune micro-environment. **A** The GO enrichment (BP, biological process) of differently expressed genes across different risk subgroups. **B** The CIBERSORT analysis revealed the proportion of 22 immune cell types in subgroups. **C**, **D** The box plot displayed the CD4+ T cell, CD8+ T cell distribution, and CD274 (encoding PD-L1) expression in risk subgroups. *p value < 0.05, **p value < 0.01, ***p value < 0.001; ns, not significant.

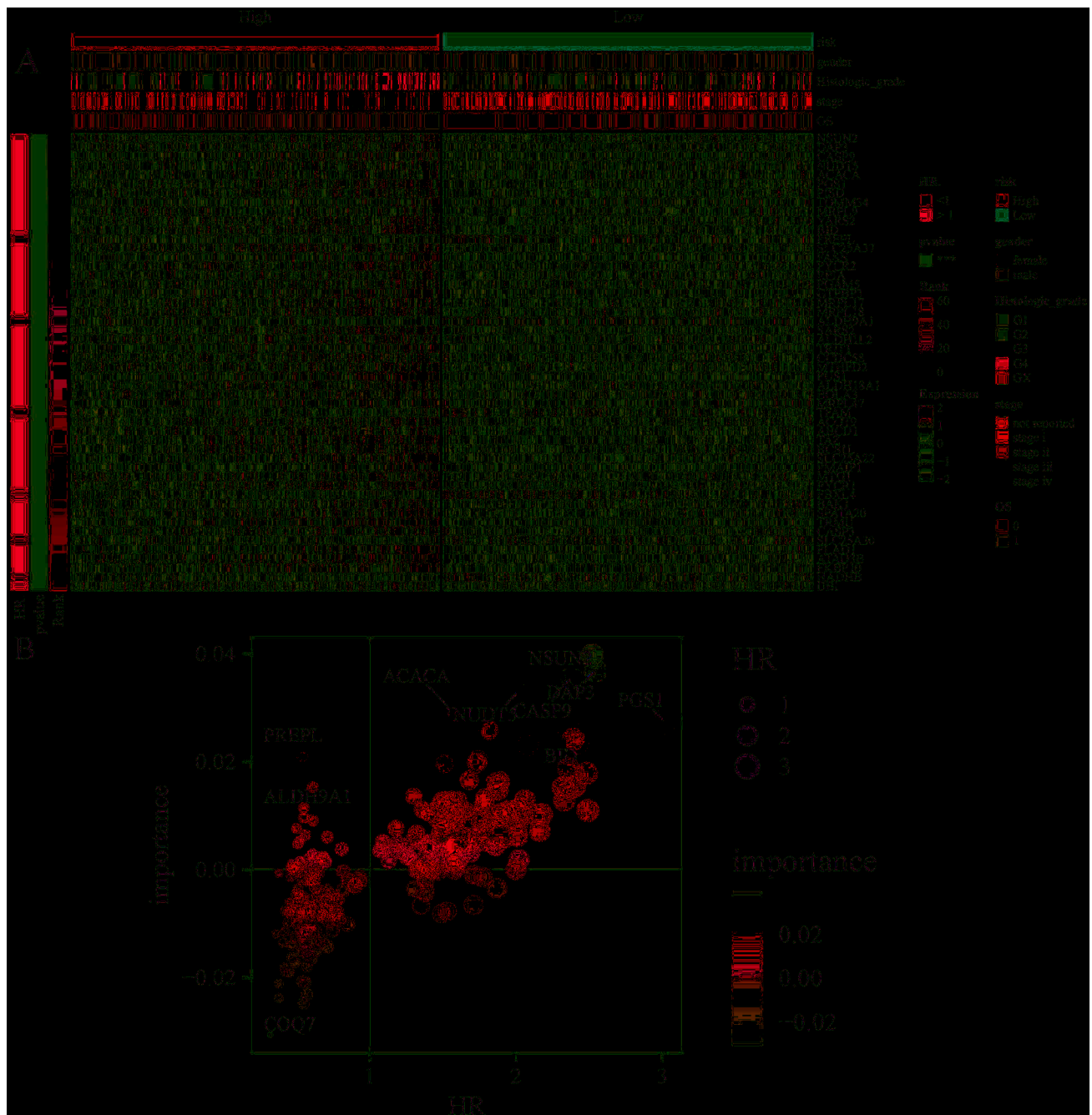


Fig. 3 Screening of the most important gene based on clinical and transcriptomic profiling. **A** The heatmap shows the mRNA expression of top 50 key genes in the Mitoscore model and their relationship with clinical stages. **B** The dot plot presented univariate Cox regression analysis and model gene's coefficient (importance). HR, hazard ratio. * p value < 0.05 , ** p value < 0.01 , *** p value < 0.001 ; ns, not significant.

histologic grade (Fig. 4E). Collectively, these findings suggest that NSUN2 is closely associated with cancer progression and may serve as a potential oncogene and prognostic biomarker.

NSUN2 bridges glycolysis to lactylation-mediated immune evasion

We investigated the gene function of NSUN2 in the mouse renal cancer cell line: Renca. CCK-8 and clone formation analysis confirmed that silencing NSUN2 resulted in decreased cell proliferation (Fig. 4F, G). Knockdown of NSUN2 also led to suppression of cell migration and invasion (Fig. 4H, I). Furthermore in metabolism, downregulated NSUN2 resulted in reduced levels of glycolysis, including the basal glycolysis level, glycolytic

capacity (defined as the maximum rate at which a cell converts glucose to pyruvate or lactate), and glycolytic reserve (the difference between basal glycolysis and glycolytic capacity) [36] (Fig. 5A–D). At the same time, ATP and lactylation levels were also downregulated (Fig. 5E, F). Consistent with previous studies, silencing NSUN2 reduced the RNA stability of NEO1, an important glycolysis enzyme (Fig. 5G), leading to a decrease in its protein levels and subsequent downregulation of glycolysis [37, 38]. Western blotting showed that NSUN2 positively regulated histone H3K18 lactylation through downregulating ENO1 (Fig. 5H).

A previous study reported glycolysis-driven H3K18 lactylation promoted CD274 transcription through TOM121/MYC signaling [39]. Thus, we aimed to investigate whether NSUN2 regulates PD-

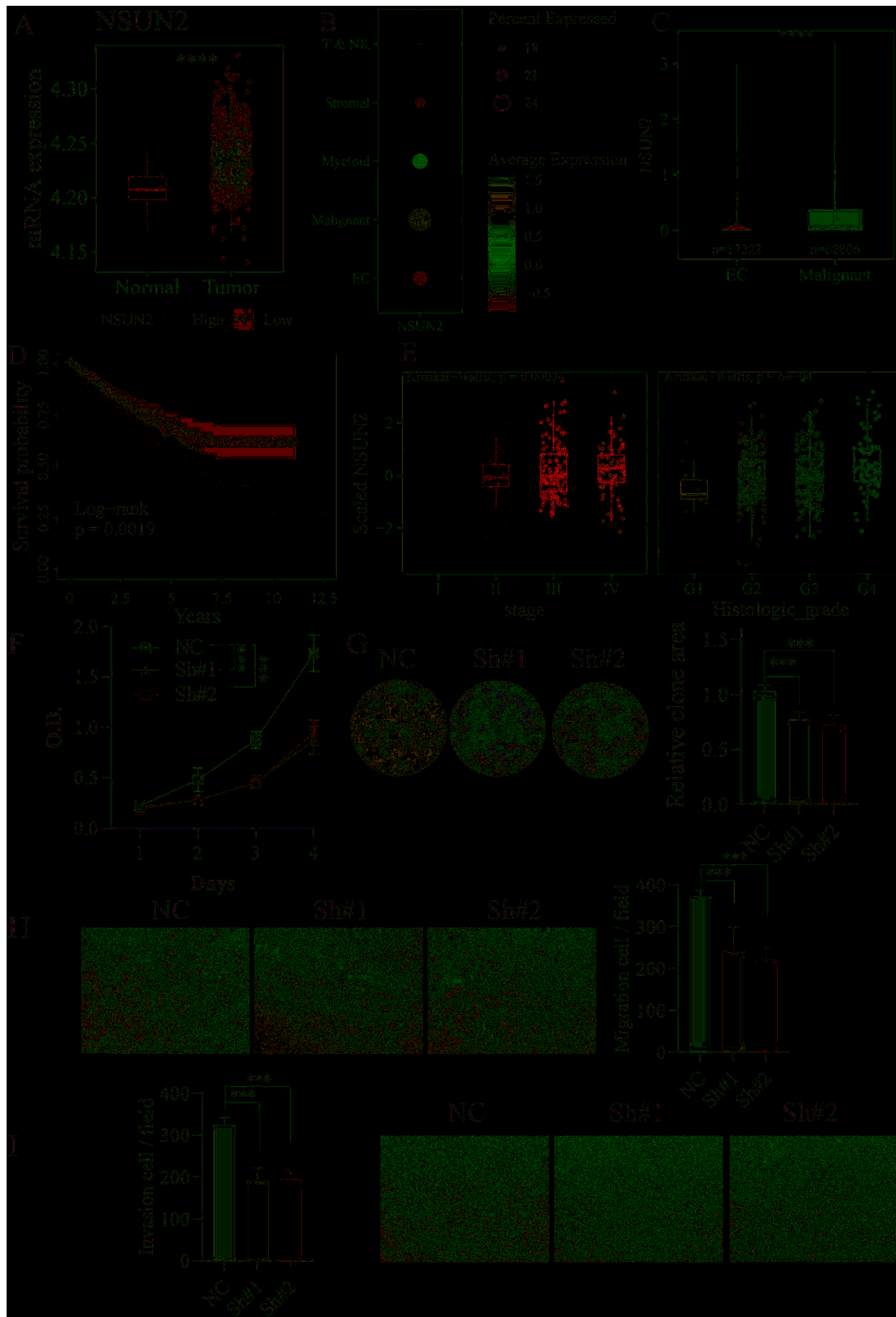


Fig. 4 The expression pattern and genetic role of NSUN2. **A** The expression level of NSUN2 in normal and tumor tissues in TCGA-KIRC dataset. **B, C** The expression of NSUN2 in single-cell dataset. **D** The survival curve of NSUN2 in TCGA-KIRC dataset. **E** The relationship between NSUN2 and clinical features (tumor stage and histologic grade) in TCGA-KIRC dataset. **F** The CCK-8 assay in normal control (NC) 786-O cells and down-regulated NSUN2 786-O cell using shRNA (short hairpin RNA). O.D., optical intensity. **G** The cell clone formation assay. **H, I** The migration and invasion experiments. * p value < 0.05 , ** p value < 0.01 , *** p value < 0.001 ; ns, not significant.

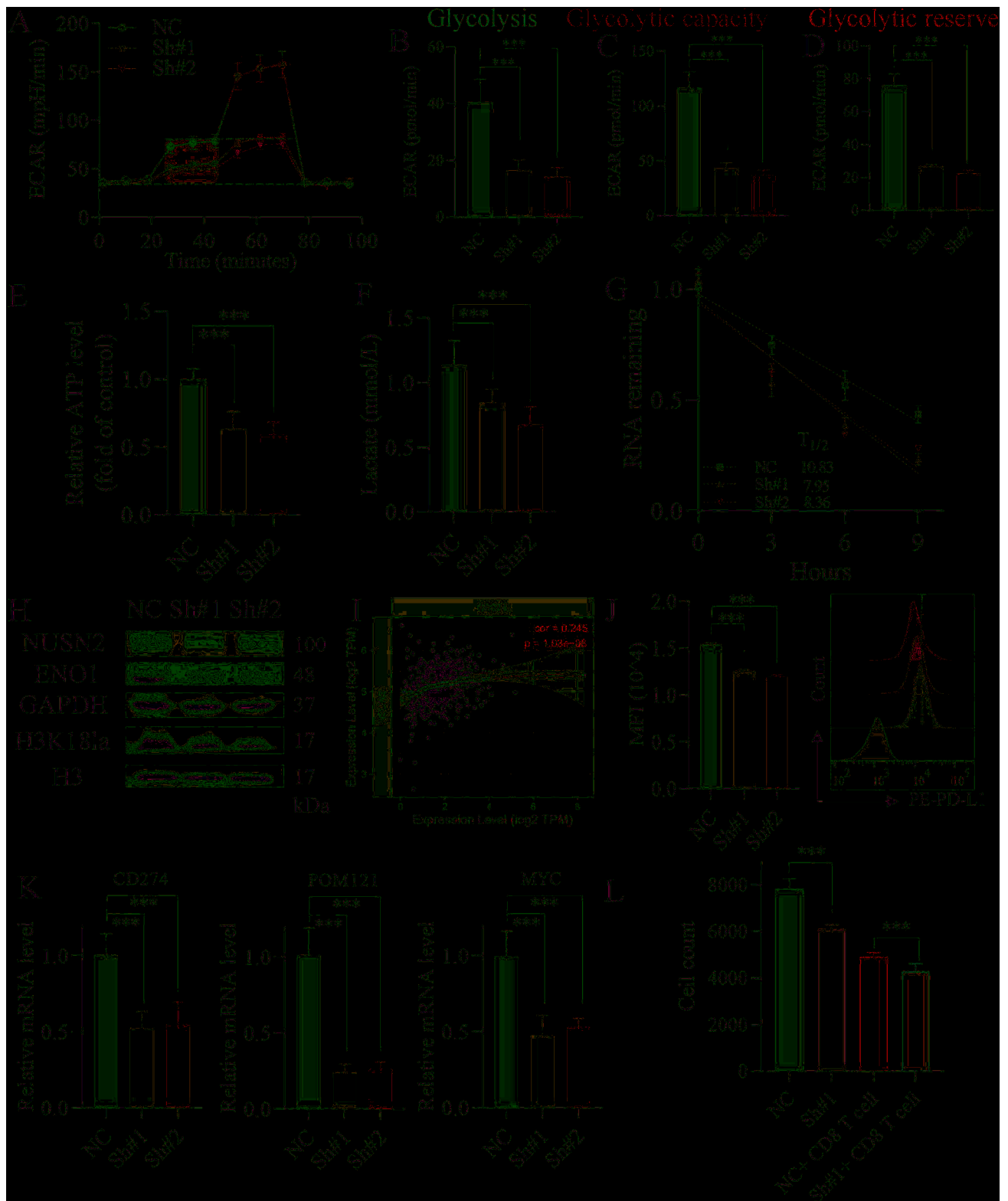


Fig. 5 NSUN2 promotes mitochondrial metabolism and PD-L1 expression. **A, B** The glycolytic rate assay (A–D) The glycolytic rate assay. The output of seahorse metabolic analyzer (A) and calculated results of glycolytic indexes (B–D). ECAR, extracellular acidification rate. **E, F** The ATP and lactate level assays. **G** The RNA stability assay of ENO1. **H** Western blotting revealed the reduced protein expression of NSUN2, ENO1, and H3K18la. **I** The mRNA expression correlation between NSUN2 and CD274 in TCGA-KIRC from TIMER database. **J** Flow cytometry detected cell membrane PD-L1 expression. MFI, mean fluorescence intensity. **K** The relative mRNA expression of CD274, POM121, and MYC. **L** The T-cell killing assay using co-culture with Renca cells and primary T cells in vitro ($n = 9$). * p value < 0.05, ** p value < 0.01, *** p value < 0.001; ns, not significant.

L1 in a lactylation-dependent manner. Here, downregulated NSUN2 reduced both protein and mRNA expression (CD274 codes PD-L1 protein) of PD-L1 (Fig. 5J, K). NSUN2 knockdown led to a deactivation of the TOM121/MYC/CD274 axis (Fig. 5K). Furthermore, the knockdown of NSUN2 promoted the tumor-killing effect of T cells in vitro (Fig. 5L). In summary, the downregulation of NSUN2 suppressed histone lactylation via NEO1-glycolysis-lactate pathway, and subsequently decreased PD-L1 expression via inhibiting TOM121/MYC/PD-L1 signaling axis, which contributed to enhanced T-cell cytotoxicity.

NSUN2 promotes tumor growth by inducing T-cell dysfunction

Further experiments in mice confirmed the in vivo genetic role of NSUN2. NSUN2 knockdown significantly reduced tumor volumes and tumor weights (Fig. 6A–C). Meanwhile, the downregulation of NSUN2 was associated with decreased tumor malignancy, as evidenced by increased tumor spacing, reduced karyokinesis, and lower Ki67 levels, indicating decreased tumor proliferation (Fig. 6D). We also evaluated the impact of NSUN2 on T cell infiltration and function in vivo. Importantly, silencing of NSUN2 improved the CD8⁺ T cell infiltration in tumor tissues (Fig. 6E). NSUN2 downregulation reduced T cell suppression, as demonstrated by increased TNF- α production in CD8⁺ T cells (Fig. 6F). Taken together, we propose a model for the molecular mechanism of NSUN2: NSUN2 promotes glycolysis and lactate accumulation, the latter leading to the lactation of the histone H3K18, which mediates immune escape by promoting PD-L1 expression via the TOM121/MYC/CD274 signaling axis (Fig. 6G).

CONCLUSIONS AND DISCUSSIONS

We collected multiple renal carcinoma cohorts (including RNA sequencing data and single-cell transcriptomics) to depict the therapeutic vulnerability and prognostic role of mitochondrial genes in renal cell carcinoma. The optimal Mitoscore model, Mitoscore, with high predictive accuracy towards prognostic status, was selected from 117 combination models based on 10 machine learning algorithms. Furthermore, immune microenvironment analysis revealed a worse immune infiltration pattern with reduced levels of anti-tumor CD4⁺ and CD8⁺ T cells and elevated expression of the immune checkpoint PD-L1 in the Mitoscore-high subgroup relative to the Mitoscore-low subgroup, which contributed to the different survival outcomes. In addition, metabolic pathway activity analysis revealed considerable heterogeneity among ccRCC patients, with Mitoscore-high tumor cells displaying increased oxidative phosphorylation, glycolytic activity, and increased glucose and lactate flux. In brief, metabolic and immune heterogeneity provide important insights into the different survival outcomes associated with Mitoscore-defined subgroups in renal cell carcinoma.

NSUN2, the most crucial gene in the Mitoscore model, was chosen for subsequent cellular and animal experiments. NSUN2 was found to be highly expressed in various tumor samples and was identified as an oncogene in several types of cancers, including lung, breast, liver, and cervical cancer [40]. NSUN2 mRNA was abnormally expressed in renal cancer cell lines and ccRCC tissue samples [41]. NSUN2 involved multiple biological processes, primarily by controlling mRNA stability, enhancing mRNA translation efficiency in the nucleus, and modulating cellular stress responses [40, 42]. Recently, NSUN2 upregulated the Wnt/ β -catenin pathway in hepatocellular carcinoma in an m5C-dependent manner [43]. Similarly, NSUN2 enhanced the stability of TIAM2, accelerating the progression of pancreatic cancer [44]. Interestingly, NSUN2, as the 5-methylcytosine (m5C) “writer”, deteriorated Th17 cell-mediated colitis by promoting m5C-modified stability of IL17 [45]. The hyperactivation of the glucose/NSUN2/TREX2 axis inhibited anti-PD-L1 immunotherapy

by suppressing the cGAS/STING signaling pathway [38]. Simultaneously, NSUN2 elevated lactate and histone lactylation in the m5C-dependent manner, and reprogrammed glycolysis metabolism in colorectal cancer via YBX1/ENO1 axis [37]. The expression of ENO1/2 (Enolase 1/2) and LDHA (Lactate dehydrogenase A), glucose, and lactate levels, were abnormally elevated in RCC tumors [15, 46]. Moreover, RCC demonstrated a greater reliance on glycolysis compared to the TCA cycle [47]. Recently, NSUN2-mediated m5C facilitated chemotherapy resistance in anaplastic thyroid cancer [48], chemotherapy in osteosarcoma [49], radiochemotherapy resistance in esophageal squamous cell carcinoma [50], and resistance of androgen receptor inhibitor in prostate cancer [51]. Similarly, NSUN2 led to gefitinib resistance depending on the NSUN2-YBX1-QSOX1 axis [52]. These studies emphasized the crucial role of NSUN2 in tumor treatment resistance. Despite these findings, the molecular role and gene function of NSUN2 in RCC is still a largely unexplored area. In our study, silenced NSUN2 resulted in significant suppression of cell proliferation, migration, and invasion. Downregulation of NSUN2 led to a reduction in the basal glycolysis level, glycolytic capacity, and glycolytic reserve [36]. NSUN2 knockdown reduced levels of ATP, lactate, and H3K18 lactylation. These findings reinforce prior reports suggesting that NSUN2 is essential for glycolytic reprogramming and subsequent histone lactylation via the NSUN2/lactate/H3K18 lactylation axis. However, further functional rescue experiments of LDHA are necessary to confirm the positive regulation of glycolysis and lactylation by NSUN2.

Tumor cells exhibit elevated expression of PD-L1, which binds to the PD-1 receptor on T cells, thereby blocking T cell activation and proliferation through suppression of the PI3K/Akt and RAS/MAPK/ERK pathway axis. This interaction ultimately facilitates tumor immune evasion [53, 54]. CD8⁺ T cells produce and secrete death-inducing granules, such as granzyme B, IFN- γ , and TNF- α , to directly eliminate tumor cells. They are widely recognized as key immune effectors and T-cell function factors in anti-tumor immunity in the tumor microenvironment [55, 56]. Glycolysis-driven H3K18 lactylation promoted PD-L1-mediated immune evasion in non-small cell lung cancer by upregulating the POM121/MYC/CD274 signaling axis [39]. In this study, NSUN2 knockdown reduced PD-L1 expression, enhancing the tumor-killing effects of primary CD8⁺ T cells in vitro. NSUN2 knockdown suppressed tumor growth and proliferation in vivo. Further flow cytometry analysis showed that NSUN2 downregulation improved the infiltration level and function of CD8⁺ T cells, indicated by increased TNF- α production. Together, NSUN2 functioned as the m5C “writer”, promoting glycolysis and H3K18 lactylation via stabilizing NEO1 mRNA, and enhanced lactylation and PD-L1 expression. Thus, NSUN2 acted as an oncogene in Renca cells by facilitating glycolysis and histone lactylation-mediated PD-L1 expression.

Although our prognostic model shows significant clinical utility, it relies on RNA sequencing data, which may not be available to cancer patients in the clinic. To address this issue, we plan to streamline the model to incorporate immunohistochemistry data. There is a need for further studies to elucidate the molecular mechanisms which NSUN2 regulates PD-L1 in renal cell carcinoma cell lines, particularly its dependence on H3K18 lactylation. There is a lack of studies on whether the NSUN2 small molecule inhibitor MY-1B can promote the efficacy of immune checkpoint blockade therapy [57]. Further validation of NSUN2 to enhance glycolysis and histone lactylation through YBX1/NEO1 signaling in an m5C-dependent manner is needed in human kidney cancer cell lines. Histone lactylation directly promotes CD274 transcription in glioblastoma cell [58], while the specific molecular mechanisms by which NSUN2 regulates the expression of PD-L1 are poorly understood, beyond just the POM121/MYC/CD274 signaling axis [39].

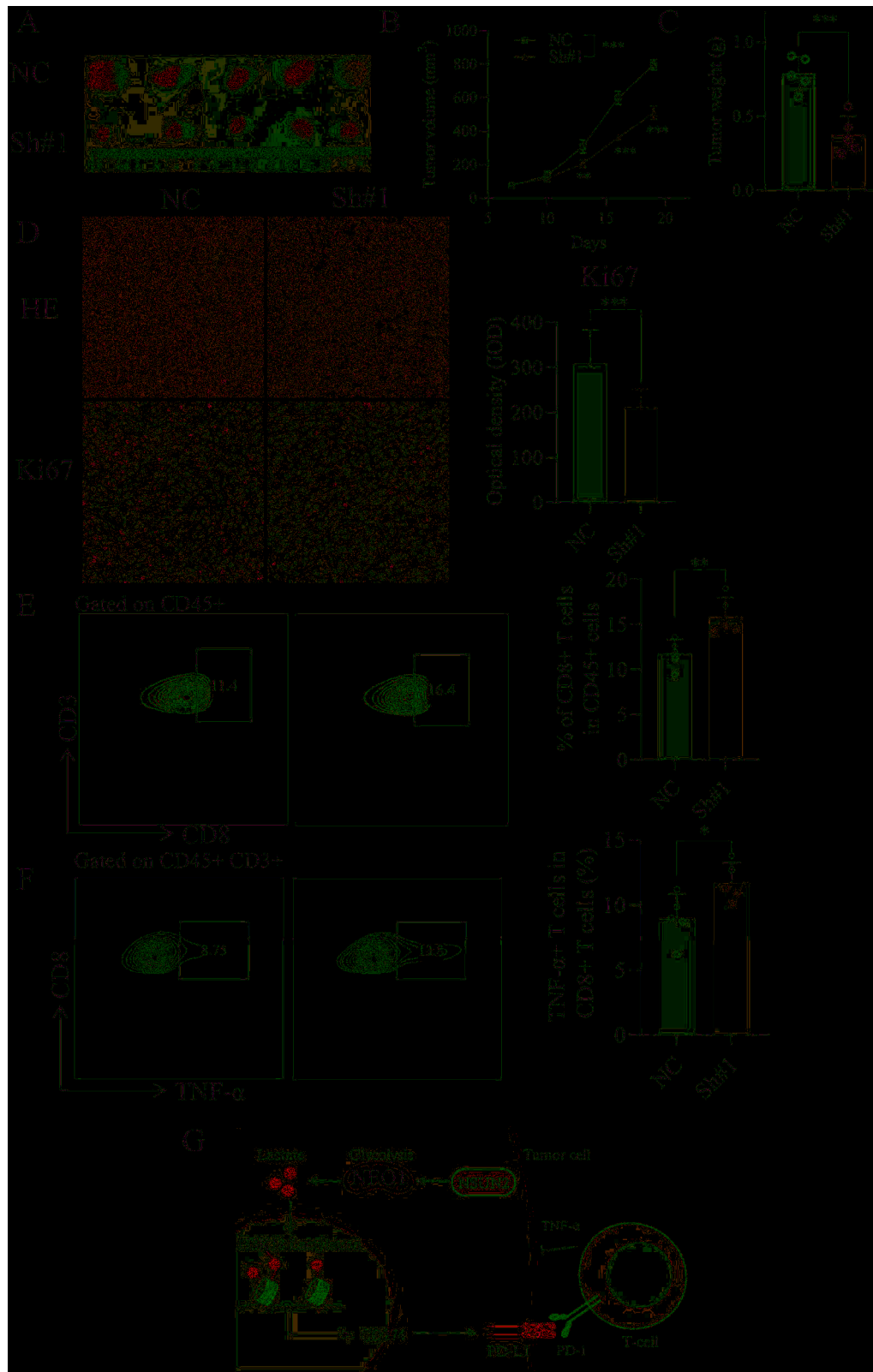


Fig. 6 NSUN2 bridges glycolysis and lactylation-mediated immune escape. **A** The picture of tumors in the normal control (NC) group and NSUN2 knockdown (Sh#1) group. **B, C** The tumor volume and weight. **D** The HE and Ki67 (proliferation marker) staining in mice tumor tissues. **E, F** Flow cytometry detected T-cell infiltration level and T-cell activation status (TNF- α) in mice tumors ($n = 5$). **G** The model of NSUN2 in renal cell carcinoma: NSUN2 promoted glycolysis that enhanced lactate production, causing cell proliferation and lactate accumulation, leading to histone lactylation-mediated H3K18 lactylation increasing PD-L1 expression, which bridged glycolysis and immune evasion. * p value < 0.05, ** p value < 0.01, *** p value < 0.001; ns, not significant.

In conclusion, we integrated bioinformatics to systematically explore the clinical features and therapeutic potential of mitochondrial genes in renal cell carcinoma. Importantly, we screened for a potential metabolic therapeutic target-NSUN2, an RNA m5C transferase, which promotes tumor cell proliferation and immune escape through the NEO1/glycolysis/histone lactylation/PD-L1 signaling axis. Our study first reveals the oncogenic role of NSUN2 in kidney cancer and highlights therapeutic vulnerability to uncouple mitochondrial metabolism and immune suppression in a histone lactylation-dependent manner, providing alternative strategies for tumor immunotherapy and even reversal of chemotherapy resistance.

DATA AVAILABILITY

All clinical cohorts and sequencing data are publicly available. The data used to support the findings of this study are available from the corresponding author on reasonable request.

CODE AVAILABILITY

The R codes are available at <https://github.com/Wanglab1986/ccRCC>.

REFERENCES

- Qu Y, Feng J, Wu X, Bai L, Xu W, Zhu L, et al. A proteogenomic analysis of clear cell renal cell carcinoma in a Chinese population. *Nat Commun*. 2022;13:2052. <https://doi.org/10.1038/s41467-022-29577-x>.
- Gong J, Maia MC, Dizman N, Govindarajan A, Pal SK. Metastasis in renal cell carcinoma: biology and implications for therapy. *Asian J Urol*. 2016;3:286–92. <https://doi.org/10.1016/j.ajur.2016.08.006>.
- Wettersten HI, Aboud OA, Lara PN, Weiss RH. Metabolic reprogramming in clear cell renal cell carcinoma. *Nat Rev Nephrol*. 2017;13:410–9. <https://doi.org/10.1038/nrneph.2017.59>.
- Linehan WM, Schmidt LS, Crooks DR, Wei D, Srinivasan R, Lang M, et al. The metabolic basis of kidney cancer. *Cancer Discov*. 2019;9:1006–21. <https://doi.org/10.1158/2159-8290.Cd-18-1354>.
- Siegel RL, Miller KD, Fuchs HE, Jemal A. Cancer statistics, 2022. *Cancer J Clin*. 2022;72:7–33. <https://doi.org/10.3322/caac.21708>.
- Murali R, Gopalakrishnan AV. Molecular insight into renal cancer and latest therapeutic approaches to tackle it: an updated review. *Med Oncol*. 2023;40:355. <https://doi.org/10.1007/s12032-022-02225-0>.
- Hwang A, Mehra V, Chhetri J, Ali S, Tran M, Roddie C. Current treatment options for renal cell carcinoma: focus on cell-based immunotherapy. *Cancers*. 2024;16:1209.
- Zhou J, Wang L, Peng C, Peng F. Co-targeting tumor angiogenesis and immunosuppressive tumor microenvironment: a perspective in Ethnopharmacology. *Front Pharm*. 2022;13:886198. <https://doi.org/10.3389/fphar.2022.886198>. Epub 2022/07/06.
- Powles T, Albiges L, Bex A, Comperat E, Grünwald V, Kanesvaran R, et al. Renal cell Carcinoma: Esmo Clinical Practice Guideline for Diagnosis, Treatment and Follow-Up. *Ann Oncol*. 2024;35:692–706. <https://doi.org/10.1016/j.annonc.2024.05.537>.
- Kuo H-Y, Khan KA, Kerbel RS. Antiangiogenic-immune-checkpoint inhibitor combinations: lessons from Phase III clinical trials. *Nat Rev Clin Oncol*. 2024;21:468–82. <https://doi.org/10.1038/s41571-024-00886-y>.
- Bui TO, Dao VT, Nguyen VT, Feugeas J-P, Pamoukdjian F, Bousquet G. Genomics of clear-cell renal cell carcinoma: a systematic review and meta-analysis. *Eur Urol*. 2022;81:349–61. <https://doi.org/10.1016/j.eururo.2021.12.010>.
- Medina López RA, Rivero Belenchon I, Mazuecos-Quirós J, Congregado-Ruiz CB, Couñago F. Update on the treatment of metastatic renal cell carcinoma. *World J Clin Oncol*. 2022;13:1–8. <https://doi.org/10.5306/wjco.v13.i1.1>. Epub 2022/02/05.
- Bi K, He MX, Bakouny Z, Kanodia A, Napolitano S, Wu J, et al. Tumor and immune reprogramming during immunotherapy in advanced renal cell carcinoma. *Cancer Cell*. 2021;39:649–61.e5. <https://doi.org/10.1016/j.ccell.2021.02.015>.
- Kroemer G, Pouyssegur J. Tumor cell metabolism: Cancer's Achilles' Heel. *Cancer Cell*. 2008;13:472–82. <https://doi.org/10.1016/j.ccr.2008.05.005>.
- Clark DJ, Dhanasekaran SM, Petralia F, Pan J, Song X, Hu Y, et al. Integrated proteogenomic characterization of clear cell renal cell carcinoma. *Cell*. 2019;179:964–83.e31. <https://doi.org/10.1016/j.cell.2019.10.007>.
- Tian J, Luo J, Zeng X, Ke C, Wang Y, Liu Z, et al. Targeting oxidative phosphorylation to increase the efficacy of immune-combination therapy in renal cell carcinoma. *J Immunother Cancer*. 2024;12:e008226. <https://doi.org/10.1136/jitc-2023-008226>.
- Bezawada D, Perelli L, Lesner NP, Cai L, Brooks B, Wu Z, et al. Mitochondrial Complex I promotes kidney cancer metastasis. *Nature*. 2024;633:923–31. <https://doi.org/10.1038/s41586-024-07812-3>.
- Chen W, Hill H, Christie A, Kim MS, Holloman E, Pavia-Jimenez A, et al. Targeting renal cell carcinoma with a Hif-2 antagonist. *Nature*. 2016;539:112–7. <https://doi.org/10.1038/nature19796>.
- Meric-Bernstam F, Tannir NM, Mier JW, DeMichele A, Telli ML, Fan AC, et al. Phase 1 Study of Cb-839, a small molecule Inhibitor of Glutaminase (Gls), alone and in combination with Everolimus (E) in Patients (Pts) with Renal Cell Cancer (RCC). *J Clin Oncol*. 2016;34:4568. https://doi.org/10.1200/JCO.2016.34.15_suppl.4568.
- Jochems C, Fantini M, Fernando RI, Kwilas AR, Donahue RN, Lepone LM, et al. The Ido1 selective inhibitor epacadostat enhances dendritic cell immunogenicity and lytic ability of tumor antigen-specific T Cells. *Oncotarget*. 2016;7:37762–72. <https://doi.org/10.18632/oncotarget.9326>.
- Jiang M, Wu S, Xie K, Zhou G, Zhou W, Bao P. The significance of Ferroptosis in renal diseases and its therapeutic potential. *Heliyon*. 2024;10:e35882. <https://doi.org/10.1016/j.heliyon.2024.e35882>.
- Yu L, Qiu Y, Tong X. Ferroptosis in renal cancer therapy: a narrative review of drug candidates. *Cancers*. 2024;16:3131.
- Rath S, Sharma R, Gupta R, Ast T, Chan C, Durham TJ, et al. Mitocarta3.0: An updated mitochondrial proteome now with sub-organelle localization and pathway annotations. *Nucleic Acids Res*. 2020;49:D1541–D7. <https://doi.org/10.1093/nar/gkaa1011>.
- Sato Y, Yoshizato T, Shiraishi Y, Maekawa S, Okuno Y, Kamura T, et al. Integrated molecular analysis of clear-cell renal cell carcinoma. *Nat Genet*. 2013;45:860–7. <https://doi.org/10.1038/ng.2699>.
- Zhang J, Bajari R, Andric D, Gerthoffert F, Lepsa A, Nahal-Bose H, et al. The International Cancer Genome Consortium Data Portal. *Nat Biotechnol*. 2019;37:367–9. <https://doi.org/10.1038/s41587-019-0055-9>.
- Liu H, Zhang W, Zhang Y, Adegboro AA, Fasoanti DO, Dai L, et al. Mime: A flexible machine-learning framework to construct and visualize models for clinical characteristics prediction and feature selection. *Comput Struct Biotechnol J*. 2024;23:2798–810. <https://doi.org/10.1016/j.csbj.2024.06.035>.
- Chen B, Khodadoust MS, Liu CL, Newman AM, Alizadeh AA. Profiling Tumor Infiltrating Immune Cells with Cibersort. In: von Stechow L, editor. *Cancer Systems Biology: Methods and Protocols*. New York, NY: Springer New York (2018). p. 243–59.
- Hu J, Wang S-G, Hou Y, Chen Z, Liu L, Li R, et al. Multi-omic profiling of clear cell renal cell carcinoma identifies metabolic reprogramming associated with disease progression. *Nat Genet*. 2024;56:442–57. <https://doi.org/10.1038/s41588-024-01662-5>.
- Watson S, Porter H, Sudbery I, Thompson R. Modification of Seurat V4 for the development of a phase assignment tool able to distinguish between G2 and mitotic cells. *Int J Mol Sci*. 2024;25:4589.
- Xie J, Deng X, Xie Y, Zhu H, Liu P, Deng W, et al. Multi-omics analysis of Disulfidptosis regulators and therapeutic potential reveals glycogen synthase 1 as a Disulfidptosis triggering target for triple-negative breast cancer. *MedComm*. 2024;5:e502. <https://doi.org/10.1002/mco2.502>.
- Xie J, Deng W, Deng X, Liang J-Y, Tang Y, Huang J, et al. Single-cell histone chaperones patterns guide intercellular communication of tumor microenvironment that contribute to breast cancer metastases. *Cancer Cell Int*. 2023;23:311. <https://doi.org/10.1186/s12935-023-03166-4>.
- Wu Y, Yang S, Ma J, Chen Z, Song G, Rao D, et al. Spatiotemporal immune landscape of colorectal cancer liver metastasis at single-cell level. *Cancer Discov*. 2022;12:134–53. <https://doi.org/10.1158/2159-8290.Cd-21-0316>.
- Alghamdi N, Chang W, Dang P, Lu X, Wan C, Gampala S, et al. A graph neural network model to estimate cell-wise metabolic flux using single-cell RNA-Seq data. *Genome Res*. 2021;31:1867–84. <https://doi.org/10.1101/gr.271205.120>. Epub 2021/07/25.
- Dou L, Lu E, Tian D, Li F, Deng L, Zhang Y. Adrenomedullin induces cisplatin chemoresistance in ovarian cancer through reprogramming of glucose metabolism. (2023) 11:169–77. <https://doi.org/10.2478/jtim-2023-0091>.
- Xie J, Yang A, Liu Q, Deng X, Lv G, Ou X, et al. Single-cell RNA sequencing elucidated the landscape of breast cancer brain metastases and identified Ifi2 as a potential therapeutic target. *Cell Prolif*. 2024;57:e13697. <https://doi.org/10.1111/cpr.13697>.
- Mookerjee SA, Nicholls DG, Brand MD. Determining maximum glycolytic capacity using extracellular flux measurements. *PLOS ONE*. 2016;11:e0152016. <https://doi.org/10.1371/journal.pone.0152016>.
- Chen B, Deng Y, Hong Y, Fan L, Zhai X, Hu H, et al. Metabolic recoding of Nsun2-mediated m5C modification promotes the progression of colorectal cancer via the Nsun2/Ybx1/M5c-Eno1 positive feedback loop. *Adv Sci*. 2024;11:2309840. <https://doi.org/10.1002/adv.202309840>.
- Chen T, Xu Z-G, Luo J, Manne RK, Wang Z, Hsu C-C, et al. Nsun2 is a glucose sensor suppressing Cgas/Sting to maintain tumorigenesis and immunotherapy

- resistance. *Cell Metab.* 2023;35:1782–98.e8. <https://doi.org/10.1016/j.cmet.2023.07.009>.
39. Zhang C, Zhou L, Zhang M, Du Y, Li C, Ren H, et al. H3k18 lactylation potentiates immune escape of non-small cell lung cancer. *Cancer Res* (2024):OF1-OF13. <https://doi.org/10.1158/0008-5472.Can-23-3513>.
 40. Li P, Huang D. Nsun2-mediated RNA Methylation: Molecular Mechanisms and clinical relevance in cancer. *Cell Signal.* 2024;123:111375. <https://doi.org/10.1016/j.cellsig.2024.111375>.
 41. Wu J, Hou C, Wang Y, Wang Z, Li P, Wang Z. Comprehensive analysis of M5c RNA methylation regulator genes in clear cell renal cell carcinoma. *Int J Genom.* 2021;2021:3803724. <https://doi.org/10.1155/2021/3803724>.
 42. Chellamuthu A, Gray SG. The RNA Methyltransferase Nsun2 and its potential roles in cancer. *Cells.* 2020;9:1758.
 43. Xing H, Gu X, Liu Y, Xu L, He Y, Xue C. Nsun2 regulates Wnt signaling pathway depending on the M5c Rna modification to promote the progression of hepatocellular carcinoma. *Oncogene* (2024). <https://doi.org/10.1038/s41388-024-03184-0>.
 44. Zhang G, Liu L, Li J, Chen Y, Wang Y, Zhang Y, et al. Nsun2 stimulates tumor progression via enhancing Tiam2 mRNA stability in pancreatic cancer. *Cell Death Discov.* 2023;9:219. <https://doi.org/10.1038/s41420-023-01521-y>.
 45. Yang W-L, Qiu W, Zhang T, Xu K, Gu Z-J, Zhou Y, et al. Nsun2 Coupling with Rorγt shapes the fate of Th17 cells and promotes colitis. *Nat Commun.* 2023;14:863. <https://doi.org/10.1038/s41467-023-36595-w>.
 46. Hakimi AA, Reznik E, Lee C-H, Creighton CJ, Brannon AR, Luna A, et al. An Integrated Metabolic Atlas of clear cell renal cell carcinoma. *Cancer Cell.* 2016;29:104–16. <https://doi.org/10.1016/j.ccell.2015.12.004>.
 47. Courtney KD, Bezwada D, Mashimo T, Pichumani K, Vemireddy V, Funk AM, et al. Isotope tracing of human clear cell renal cell carcinomas demonstrates suppressed glucose oxidation in vivo. *Cell Metab.* 2018;28:793–800.e2. <https://doi.org/10.1016/j.cmet.2018.07.020>.
 48. Li P, Wang W, Zhou R, Ding Y, Li X. The M5c Methyltransferase Nsun2 promotes codon-dependent oncogenic translation by stabilising tRNA in anaplastic thyroid cancer. *Clin Transl Med.* 2023;13:e1466. <https://doi.org/10.1002/ctm2.1466>.
 49. Shao D, Liu C, Wang Y, Lin J, Cheng X, Han P, et al. Dnmt1 determines Osteosarcoma cell resistance to apoptosis by associatively modulating DNA and mRNA Cytosine-5 Methylation. *FASEB J.* 2023;37:e23284. <https://doi.org/10.1096/fj.202301306R>.
 50. Niu X, Peng L, Liu W, Miao C, Chen X, Chu J, et al. A Cis-Eqlt in Nsun2 promotes esophageal squamous-cell carcinoma progression and radiochemotherapy resistance by mRNA-M5c methylation. *Signal Transduct Target Ther.* 2022;7:267. <https://doi.org/10.1038/s41392-022-01063-2>.
 51. Zhu W, Wan F, Xu W, Liu Z, Wang J, Zhang H, et al. Positive epigenetic regulation loop between Ar and Nsun2 promotes prostate cancer progression. *Clin Transl Med.* 2022;12:e1028. <https://doi.org/10.1002/ctm2.1028>.
 52. Wang Y, Wei J, Feng L, Li O, Huang L, Zhou S, et al. Aberrant M5c hypermethylation mediates intrinsic resistance to Gefitinib through Nsun2/Ybx1/Qsox1 Axis in Egfr-Mutant non-small-cell lung cancer. *Mol Cancer.* 2023;22:81. <https://doi.org/10.1186/s12943-023-01780-4>.
 53. Shen S, Hong Y, Huang J, Qu X, Sooranna SR, Lu S, et al. Targeting Pd-1/Pd-L1 in tumor immunotherapy: mechanisms and interactions with host growth regulatory pathways. *Cytokine Growth Factor Rev.* 2024;79:16–28. <https://doi.org/10.1016/j.cytogfr.2024.08.001>.
 54. Zhou J, Wan F, Wang L, Peng C, Huang R, Peng F. Stat4 facilitates Pd-L1 level Via Il-12r/Jak2/Stat3 axis and predicts immunotherapy response in breast cancer. *MedComm.* 2023;4:e464. <https://doi.org/10.1002/mco2.464>.
 55. Raskov H, Orhan A, Christensen JP, Gögenur I. Cytotoxic Cd8+ T cells in cancer and cancer immunotherapy. *Br J Cancer.* 2021;124:359–67. <https://doi.org/10.1038/s41416-020-01048-4>.
 56. Koh C-H, Lee S, Kwak M, Kim B-S, Chung Y. Cd8 T-cell subsets: heterogeneity, functions, and therapeutic potential. *Exp Mol Med.* 2023;55:2287–99. <https://doi.org/10.1038/s12276-023-01105-x>.
 57. Tao Y, Felber JG, Zou Z, Njomen E, Remsberg JR, Ogasawara D, et al. Chemical proteomic discovery of isotype-selective covalent inhibitors of the RNA Methyltransferase Nsun2. *Angew Chem Int Ed.* 2023;62:e202311924. <https://doi.org/10.1002/anie.202311924>.
 58. Zhu R, Ye X, Lu X, Xiao L, Yuan M, Zhao H, et al. Acss2 acts as a Lactyl-CoA Synthetase and couples Kat2a to function as a lactyltransferase for histone lactylation and tumor immune evasion. *Cell Metab* (2024). <https://doi.org/10.1016/j.cmet.2024.10.015>.

ACKNOWLEDGEMENTS

Thanks to the researchers and patients for contributing to public databases. All reviewers and editors are thanked for their contributions.

AUTHOR CONTRIBUTIONS

KW, FK, XH: Conceptualization and Investigation Writing. YZ: Writing– review & editing. Hui Wang, Hai Wang and CR: Writing– review & editing, Supervision.

FUNDING

This study was supported by the Lianyungang City Health Science and Technology Project (Grant No. 202409) and the Scientific Development Fund of Xuzhou Medical University Affiliated Hospital (Grant No. XYFM202456).

COMPETING INTERESTS

The authors declare no competing interests.

ETHICS

The Animal Ethics Committee of the Affiliated Lianyungang Hospital of Xuzhou Medical University approved the studies involving animals (Approved ID: KY-20210910004).

ADDITIONAL INFORMATION

Supplementary information The online version contains supplementary material available at <https://doi.org/10.1038/s41435-025-00336-4>.

Correspondence and requests for materials should be addressed to Hai Wang, Chuanli Ren or Hui Wang.

Reprints and permission information is available at <http://www.nature.com/reprints>

Publisher's note Springer Nature remains neutral with regard to jurisdictional claims in published maps and institutional affiliations.

Springer Nature or its licensor (e.g. a society or other partner) holds exclusive rights to this article under a publishing agreement with the author(s) or other rightsholder(s); author self-archiving of the accepted manuscript version of this article is solely governed by the terms of such publishing agreement and applicable law.